The Astrophysical Journal, 954:179 (14pp), 2023 September 10 https://doi.org/10.3847/1538-4357/ace7bb

Fast Radio Bursts as Probes of Magnetic Fields in Galaxies at $z < 0.5$

Alexandra G. Mannings[1], Rüdiger Pakmor[2], J. Xavier Prochaska[1,3,4], Freeke van de Voort[5], Sunil Simha[1], R. M. Shannon[6], Nicolas Tejos[7], Adam Deller[6], and Marc Rafelski[8,9]
[1] Department of Astronomy and Astrophysics, University of California, Santa Cruz, CA 95064, USA; almannin@ucsc.edu
[2] Max Planck Institute for Astrophysics, Karl-Schwarzschild-Str. 1, D-85741 Garching, Germany
[3] Kavli Institute for the Physics and Mathematics of the Universe (Kavli IPMU), 5-1-5 Kashiwanoha, Kashiwa 277-8583, Japan
[4] Division of Science, National Astronomical Observatory of Japan, 2-21-1 Osawa, Mitaka, Tokyo 181-8588, Japan
[5] Cardiff Hub for Astrophysics Research and Technology, School of Physics and Astronomy, Cardiff University, Queen's Buildings, The Parade, Cardiff, CF24 3AA, UK
[6] Centre for Astrophysics and Supercomputing, Swinburne University of Technology, Hawthorn, VIC 3122, Australia
[7] Instituto de Física, Pontificia Universidad Católica de Valparaíso, Casilla 4059, Valparaíso, Chile
[8] Space Telescope Science Institute, Baltimore, MD 21218, USA
[9] Department of Physics and Astronomy, Johns Hopkins University, Baltimore, MD 21218, USA
Received 2022 October 3; revised 2023 July 11; accepted 2023 July 14; published 2023 September 6

Abstract

We present a sample of nine fast radio bursts (FRBs) from which we derive magnetic field strengths of the host galaxies represented by normal, $z < 0.5$ star-forming galaxies with stellar masses $M_* \approx 10^8$–$10^{10.5}\ M_\odot$. We find no correlation between the FRB rotation measure (RM) and redshift, which indicates that the RM values are due mostly to the FRB host contribution. This assertion is further supported by a significant positive correlation (Spearman test probability $P_S < 0.05$) found between the RM and the estimated host dispersion measure ($\mathrm{DM_{host}}$; with Spearman rank correlation coefficient $r_S = +0.75$). For these nine galaxies, we estimate their magnetic field strengths projected along the sight line $|B_\parallel|$, finding a low median value of 0.5 μG. This implies the magnetic fields of our sample of hosts are weaker than those characteristic of the solar neighborhood ($\approx 6\ \mu$G), but relatively consistent with a lower limit on the observed range of $\approx$2–10 μG for star-forming disk galaxies, especially as we consider reversals in the B-field, and that we are only probing $\mathrm{B_\parallel}$. We compare to RMs from simulated galaxies of the Auriga project—magneto-hydrodynamic cosmological zoom simulations—and find that the simulations predict the observed values to within a 95% confidence interval. Upcoming FRB surveys will provide hundreds of new FRBs with high-precision localizations, RMs, and imaging follow-up to support further investigation into the magnetic fields of a diverse population of $z < 1$ galaxies.

Unified Astronomy Thesaurus concepts: Radio transient sources (2008); Galaxy evolution (594); Extragalactic magnetic fields (507)

1. Introduction

Fast radio bursts (FRBs) are millisecond-duration pulses of radio emission, arising predominantly from extragalactic sources (e.g., Cordes & Chatterjee 2019). The first burst discovered, subsequently named the Lorimer burst (Lorimer et al. 2007), revealed a new radio transient class with unprecedented power to probe cosmological questions of matter distribution, universal expansion, and (inter-)galactic magnetism due to their dispersion and rotation measures (DMs, RMs; e.g., Gaensler 2009; Macquart et al. 2010; Akahori & Ryu 2011; Macquart et al. 2015; Akahori et al. 2016). Since the discovery of FRBs, their DM has already been used to search for answers to long-standing questions. Works such as Macquart et al. (2020) and Simha et al. (2020) offer a nearly complete baryon census—finding baryons where they were once nearly impossible to detect. Galactic halos and the intergalactic medium (IGM) are now being backlit by the flashlights that are FRBs, illuminating the once "missing" matter.

FRBs also have potential to probe another influential property of the Universe: magnetic fields (e.g., Piro & Gaensler 2018; Hackstein et al. 2019). Many questions such as the origins of magnetic fields, their effects on the evolution of galaxies, and the process of their amplification over cosmological time have been explored extensively with theoretical treatments (e.g., Springel 2010; Pakmor et al. 2011; Rodrigues et al. 2018). Observational constraints, however, are currently scant and are critically needed to constrain the physical processes at work.

There are a number of ways to measure the effects of magnetism in galactic and extragalactic systems, and each method is sensitive to a different magnetic field component (see Beck 2015 for a list of magnetic field components and observational methods). The Zeeman effect can be observed in the emission-line spectra of galaxies, indicating a regular field along the line of sight. One can also measure the polarized intensity and linear polarization angle of QSOs and other persistent radio sources, or evaluate signatures from synchrotron radiation, which are associated with the magnetic field component perpendicular to the line of sight.

In this study, we use the Faraday RMs, which quantify the effect of magnetized plasma on linearly polarized radiation, of FRBs to probe the component of the magnetic field that is parallel to the line of sight ($B_\parallel$). This measure can elucidate the magneto-ionic environment surrounding the FRB. As the signal also interacts with the IGM and circumgalactic medium (CGM)

of the FRB host, we can make measurements of the fields in these broader regions as well.

Constraining these field components helps determine what processes are implicated in the production and amplification of magnetic fields—whether tied to the progenitor object itself and its immediate environment (e.g., Piro & Gaensler 2018) or evolution on galactic and cosmic scales (e.g., Hackstein et al. 2019). Comparison of the observed quantities to those predicted by simulations can be an invaluable test of our understanding of the relationship between magnetic fields and galaxy evolution (e.g., Rodrigues et al. 2018). We can also test FRB progenitor models and how burst properties would be affected.

In this paper, we make use of the Auriga simulations (Grand et al. 2017), a set of high-resolution cosmological zoom-in simulations of Milky Way–like galaxies that reproduce many important properties of their observed counterparts. In particular, they include a self-consistent model of magnetic field amplification and evolution over cosmic time that produces realistic magnetic field strengths at $z = 0$ (Pakmor et al. 2017, 2018, 2020). We use the simulations to connect the FRB observations to conditions in their local and global environments of their host galaxies.

We also explore the possible connections between the RMs of a set of FRBs and local characteristics, as determined by, e.g., Bhandari et al. (2020a), Heintz et al. (2020), and Mannings et al. (2021). These works demonstrate that FRBs originate primarily in star-forming galaxies with stellar masses ranging from $M_* \sim 10^8$–10^{11} $M_\odot$. These data also reveal the location of the FRBs within their hosts and constrain local measures such as the star formation density, which may correlate with magnetized plasma.

This paper is organized as follows. We describe the RM in detail in Section 1.1. In Section 2, we outline the selection criteria for our sample (Section 2.1), provide a description of RM data (Section 2.2), detail the host observations for each burst (Section 2.3), and describe host properties (Section 2.4). In Section 3, we discuss the observational analysis and results. We begin by detailing the methods for estimating host contributions to RM and DM ($\mathrm{RM_{host}}$ and $\mathrm{DM_{host}}$), including the extragalactic contribution to the RM (Section 3.1), the Milky Way contribution to the RM (Section 3.1.1), the correlation between RM and redshift (Section 3.1.2), and estimates of $\mathrm{DM_{host}}$ (Section 3.2). We then investigate correlations between host-galaxy characteristics in Section 3.3 and, in Section 3.4, we make estimates of magnetic field magnitudes of the galaxies hosting the FRBs. We then discuss the modeling framework and results for a magneto-hydrodynamic model of Milky Way–like galaxies (Section 4.2) with which we simulate RM and DM measurements and compare against observed values (Sections 4.3 and 4.4). We finish with a final summary and discussion of implications in Section 5.

1.1. Polarization and Faraday Effect

If the oscillations of an electromagnetic (EM) field have a preferred orientation, then this radiation is polarized. The polarization of an EM wave is determined by the orientation of the electric field component. In general, the polarization of an EM wave is elliptical, i.e., the electric field vector traces an ellipse perpendicular to the propagation direction during transit. Elliptically polarized light can be expressed as a linear combination of two orthogonal linear polarization states or two circular polarization states (Griffiths 2013). One requires only three independent parameters to describe the polarization state of an EM wave.

The polarization of radio waves, however, is most often described using the Stokes I, Q, U, and V parameters, where I refers to the total intensity, Q and U the linear polarization, and V the circular polarization. These parameters can be combined to represent polarization in the form of the Stokes vector:

$$\boldsymbol{S} = \begin{pmatrix} I \\ Q \\ U \\ V \end{pmatrix}. \tag{1}$$

Estimating Q, U, and V from raw data depends on the specific configuration of the instrument used to detect and measure the polarization signals. As we are including FRBs from multiple experiments across multiple telescopes, descriptions of their methods and parameter formulations can be found in their respective studies (Michilli et al. 2018; C. K. Day et al. 2020; Mckinven et al. 2021; Kumar et al. 2022).

The linear polarization angle, ψ, is expressed as

$$\psi = \frac{1}{2} \arctan \frac{U}{Q} \ . \tag{2}$$

ψ is, in general, a function of frequency and time, $\psi(\nu, t)$, and for FRBs it has been observed to evolve over the duration of the burst (e.g., Michilli et al. 2018; C. K. Day et al. 2020, in preparation).

As monochromatic light propagates through plasma that has a magnetic field component along the direction of propagation, its linear polarization angle is rotated. The degree of rotation is proportional to the inverse square of the frequency, and the proportionality constant depends on the properties of the intervening magnetized medium. While the net rotation at any wavelength or frequency cannot be determined, for a multi-frequency radio signal, such as an FRB, the RM encodes the properties of the intervening medium and is measured from the variation of the linear polarization angle with wavelength squared:

$$\mathrm{RM} = \frac{d\psi}{d\lambda^2} \ . \tag{3}$$

For a pulse of radiation emitted at redshift z that traverses to Earth, we may express it as

$$\mathrm{RM} = C_R \int_z^0 \frac{n_e(z) B_\parallel(z)}{(1+z)2} \frac{dl(z)}{dz} dz \ \mathrm{rad\ m^{-2}}, \tag{4}$$

where C_R is a set of physical constants including the inverse square of the electron mass m_e^{-2}, the electron charge cubed e^3, and the inverse of the speed of light to the fourth power c^{-4}. n_e is the electron density, $B_\parallel$ is the magnitude of the line-of-sight magnetic field, and the integral is over the length of the sight line dl with n_e, $B_\parallel$, and dl as functions of z. RM can be positive or negative depending on the direction of the magnetic field component. In other words, RM is the average parallel magnetic field strength along the line of sight weighted by n_e. For FRBs, this includes contributions from the Milky Way, cosmic magnetic fields, and the magnetic fields within its host galaxy.

Table 1
FRB Properties and Local Characteristics

FRB	RM_{FRB} (rad m^{-2})	DM_{FRB} (pc cm^3)	z	$\delta R/r_e$	Σ_{M*} (10^8 $M_\odot$ kpc^{-2})	Σ_{SFR} ($M_\odot$ yr^{-1} kpc^{-2})	Refs
20121102A†	102700 ± 100	558	0.193	0.366 ± 0.032	0.1304 ± 0.0023	4.09 ± 0.82	(1),(2)
20180916B†	-114.60 ± 0.60	349	0.034	0.8972 ± 0.0032	0.114992 ± 0.000021	⋯	(2),(3),(4)
20180924B	22.0 ± 2.0	362	0.321	1.20 ± 0.38	0.810 ± 0.010	<0.006	(2),(5)
20190102C	-105.0 ± 1.0	365	0.291	0.45 ± 0.84	0.0930 ± 0.0021	<0.016	(2),(6)
20190608B	353.0 ± 2.0	340	0.118	0.88 ± 0.11	0.3398 ± 0.0011	0.0069 ± 0.0014	(2),(6)
20190711A†	9.0 ± 2.0	588	0.522	0.6 ± 1.8	0.0448 ± 0.0038	<0.016	(2),(6)
20191001A	55.50 ± 0.90	508	0.234	2.00 ± 0.14	0.3219 ± 0.0070	<0.005	(2),(7)
20200120E†	-29.80 ± 0.50	88	0.001	1.607 ± 0.051	⋯	⋯	(8)
20201124A†	-613.0 ± 2.0	411	0.098	0.666 ± 0.013	⋯	⋯	(9)

Notes. FRB is the TNS name of the fast radio burst; those with a dagger are known to repeat. RM_{FRB} is the rotation measure of the FRB. DM_{FRB} is the dispersion measure of the FRB rounded to the nearest whole number. Uncertainties are generally less than 1 pc cm^{-3}. z is the redshift of the FRB. $\delta R/r_e$ is the physical offset of the FRB from the host-galaxy center in units of effective radii (host-normalized offset). Σ_{M*} is the stellar mass surface density of the host galaxy at the FRB location. Σ_{SFR} is the specific star formation rate of the host galaxy at the FRB location. FRBs without Σ_{SFR} or Σ_{M*} values do not have imaging necessary to compute these quantities, and were not reported in Mannings et al. (2021). Refs are the references, as follows: (1) Michilli et al. (2018); (2) Mannings et al. (2021); (3) Tendulkar et al. (2020); (4) CHIME/FRB Collaboration et al. (2019); (5) Bannister et al. (2019); (6) Day et al. (2020); (7) Bhandari et al. (2020b); (8) Bhardwaj et al. (2021); (9) Kumar et al. (2022).

However, it is assumed the field undergoes numerous reversals along the line of sight that minimize the IGM contribution to the RM relative to the host and Milky Way contributions. Our assumptions about the structure of the magnetic field means that our interpretations of RM and derived quantities become model dependent. Nonetheless, there exist measurements of RM in cosmic filaments (RM_f) such as those presented in Carretti et al. (2022), which provide estimates around $RM_f = 0.71 \pm 0.07$ rad m^{-2}. They then infer the magnetic field magnitude in the filaments to be $B_f \approx 32$ nG. This value being a tenth of an RM unit (and assuming the value in cosmic voids is even lower due to a lack of ionized material in these regions) motivates an expectation for minimal RM contribution from the IGM. Specific to FRBs, upper limits on the CGM and IGM contributions to FRB RMs can be found in Ravi et al. (2016), Prochaska et al. (2019), and O'Sullivan et al. (2020).

Maps of the Milky Way's magnetic field and Faraday rotation have been developed using measurements of extragalactic polarized sources, as discussed in Section 3.1.1. Once this contribution is subtracted, we can isolate the other components in an effort to better understand magnetic field generation and amplification in the Universe, as well as the magneto-ionic environments of FRB progenitors.

2. Fast Radio Burst Data and Sample Selection

2.1. Selection Criteria

Presently, there are over 600 FRBs in the published literature, and of these ∼20 with published RM values. These form the parent sample from which we construct a subset for our analysis. Our scientific foci are as follows:

1. Study correlations between local host properties and the inferred host contribution to the RM.
2. Estimate magnetic fields in FRB hosts.
3. Make comparisons to cosmological zoom-in simulations that study the relationship between galaxy evolution and magnetic fields.

These scientific goals helped define the following selection criteria that each FRB must satisfy:

1. A precisely measured RM value.
2. A kiloparsec-scale FRB localization precision.
3. A high-probability association to a host galaxy.
4. A spectroscopic redshift measurement for the host galaxy.
5. Host-galaxy imaging and subsequent derived host properties, such as stellar mass, star formation rate, etc.
6. Considered and added to the sample by 2022 January.

The first criterion is fundamental to the analysis. The second addresses the fact that RMs are sensitive to turbulent small-scale magnetic fields as well as large-scale ordered fields. Requiring kiloparsec-scale localizations allows an exploration of correlations between local measures such as the star formation rate surface density and RM. In the following analysis, we require the net localization uncertainty (statistical and systematic error) be less than 5 kpc at the redshift of the host galaxy.

Regarding the third criterion, we adopt the probabilistic association of transients to hosts formalism (also known as PATH; Aggarwal et al. 2021) and demand that the FRB posterior probability $P(O|x)$ exceeds 95%. In general, this criterion is redundant along with the second, as a highly precise localization will generally yield a secure association provided sufficiently deep imaging (Eftekhari et al. 2020). The fifth and sixth criteria allow us to search for correlations between the host-galaxy properties and RM.

After applying these selection criteria to the full set of published sources, we recover nine FRBs satisfying the full set. These are listed in Table 1.

2.2. Rotation Measures and Other Burst Properties

The nine FRBs defining our sample are drawn primarily from two FRB surveys. The first is the Commensal Real-time ASKAP Fast Transients (CRAFT) survey using the Australian Square Kilometre Array Pathfinder (ASKAP) telescope (Macquart et al. 2010). The CRAFT collaboration discovered and observed six of the FRB events presented in this paper, on dates in accordance with the Transient Name Server (TNS) name of the event: 20180924B (Bannister et al. 2019), 20190102C, 20190608B, 20190711A (Day et al. 2020),

Table 2
Host Properties

FRB	R.A.$_{\rm FRB}$	Decl.$_{\rm FRB}$	R.A.$_{\rm Host}$	Decl.$_{\rm Host}$	M_* ($10^9\ M_\odot$)	SFR ($M_\odot\ {\rm yr}^{-1}$)	r_e (kpc)
20121102A†	82.9946	33.1479	82.9945	33.1479	0.143 ± 0.066	0.13	2.05 ± 0.11
20180916B†	29.5031	65.7168	29.5012	65.7147	2.15 ± 0.33	0.06	6.009 ± 0.012
20180924B	326.1052	−40.9000	326.1052	−40.9002	13.2 ± 5.1	0.88	2.82 ± 0.53
20190102C	322.4157	−79.4757	322.4149	−79.4757	4.7 ± 5.4	0.86	5.01 ± 0.15
20190608B	334.0199	−7.8982	334.0204	−7.8989	11.6 ± 2.8	0.69	7.373 ± 0.059
20190711A†	329.4192	−80.3580	329.4192	−80.3581	0.81 ± 0.29	0.42	2.48 ± 0.13
20191001A	323.3513	−54.7477	323.3518	−54.7485	46 ± 19	8.07	5.550 ± 0.029
20200120E†	149.4778	68.8189	148.8882	69.0653	72 ± 17	0.89	12.50 ± 0.40
20201124A†	77.0146	26.0607	77.0145	26.0605	2.80 ± 0.50	2.10	1.988 ± 0.037

Note. FRB is the TNS name of the fast radio burst; those with a dagger are known to repeat. R.A.$_{\rm FRB}$, decl.$_{\rm FRB}$ are the coordinates of the FRB. R.A.$_{\rm Host}$, decl.$_{\rm Host}$ are the coordinates of the host galaxy. M_* is the stellar mass of the host galaxy. SFR is the star formation rate of the host galaxy, with typical uncertainty of 30% (systematic). r_e is the effective radius of the host galaxy.

20191001A (Bhandari et al. 2020b), and 20201124A (Kumar et al. 2022). 20190711A and 20201124A are repeating bursts whose RMs may change with time; the quoted RMs are taken from the publications that these data are presented in, which are the first detected burst and an average over all detected bursts, respectively.

Two of the bursts in this sample were detected and characterized by the Canadian Hydrogen Intensity Mapping Experiment (CHIME)/FRB Experiment (FRBs 20180916B, 20200120E). The RM for FRB 20180916B, located in a nearby spiral galaxy (Tendulkar et al. 2020), is presented by the CHIME collaboration with seven other new (at the time) repeating FRBs (CHIME/FRB Collaboration et al. 2019). The RM for this burst was derived from baseband data collected on FRB 20181226A, a subsequent repetition of FRB 20180916B. FRB 20200120E is localized to a globular cluster located in the halo of M81 and is presented in Bhardwaj et al. (2021).

Lastly, we include the source commonly referred to as "The Repeater," or R1: FRB 20121102A. The RM for FRB 20121102A was first presented in Michilli et al. (2018), which detailed the extreme magneto-ionic environment in which the burst progenitor must be embedded in order to produce such a high RM, ${\rm RM_{FRB}} \sim 10^5\ {\rm rad\ m^{-2}}$. Since this is a repeating burst, we take the average quoted in Michilli et al. (2018) as our value.

Five out of the nine FRBs in this sample repeat, leaving four apparently non-repeating bursts. The sample has a median $|{\rm RM_{FRB}}| = 56\ {\rm rad\ m^{-2}}$ with a range $9\ {\rm rad\ m^{-2}} < |{\rm RM_{FRB}}| < 10^5\ {\rm rad\ m^{-2}}$ (see Table 1).

Repeating bursts can show variability and evolution over the individual burst envelope and with time over subsequent burst repetitions (e.g., Michilli et al. 2018). All of the repeating bursts in the sample show at least slight variability in their RMs from burst to burst. These variations are insignificant in comparison to the FRB source to FRB source variation in RM and do not impact any of the analysis presented here.

2.3. Host Observations

Nearly all of the observations of the host galaxies for our RM sample have been published previously. Here, we briefly review the primary data sets.

Regarding imaging, where available we have leveraged high-spatial-resolution data obtained with the Hubble Space Telescope (HST). Six of the hosts in the sample were observed by HST and its Wide-Field Camera 3 in UVIS and IR images (F300X and F160W filters, respectively) taken as part of GO programs 15878 (PI: Prochaska) and 16080 (PI: Mannings).

These programs targeted galaxies for which FRB events had been detected and localized by the CRAFT survey. These images were previously published in Chittidi et al. (2020) and Mannings et al. (2021). Information for FRBs 20180924B, 20190102C, 20190608B, 20190711A, and 20191001A was drawn from this data set.

We also include HST images from GO program 14890 (PI: Tendulkar), which observed the host of FRB 20121102A (Bassa et al. 2017). These observations include images taken in the F110W and F160W IR filters (equivalent to the J and H bands, respectively), and a narrowband Hα image with the F763M filter. Detailed descriptions of image processing and reduction can be found in Bassa et al. (2017) and Mannings et al. (2021).

The high-spatial-resolution imaging is complemented by multiband, ground-based images from public surveys and directed follow-up campaigns. We refer the reader to Heintz et al. (2020) and Bhandari et al. (2020a, 2020b, 2022) for details and note the data are all taken from the FRB repository on GitHub (Prochaska et al. 2019).

2.4. Host Properties

Central to our study is an exploration of the properties of the galaxies hosting the FRBs, both global and local measures. We use the quantities derived from previous studies throughout this work: star formation rates (global and local to the FRB, SFR, and $\Sigma_{\rm SFR}$), effective radii (r_e), stellar mass (global M_* and local Σ_{M*} to the FRB), and offsets. These are tabulated in Tables 1 (local properties) and 2 (global galaxy properties).

Figure 1 shows the locations of the FRBs within their host galaxies relative to the host-galaxy centroid and in units of r_e. We have deprojected the offsets along the major and minor axes using fits to each host with the `galfit` (Peng et al. 2010) software package, most of which are reported in Mannings et al. (2021), with the remaining two fits being presented here (FRBs 20200120E and 20201124A).

We observe that most of the bursts are located within $\approx 1.5 r_e$ from the centers of their hosts, with one burst residing further out in its host's disk at $\approx 3 r_e$. Furthermore,

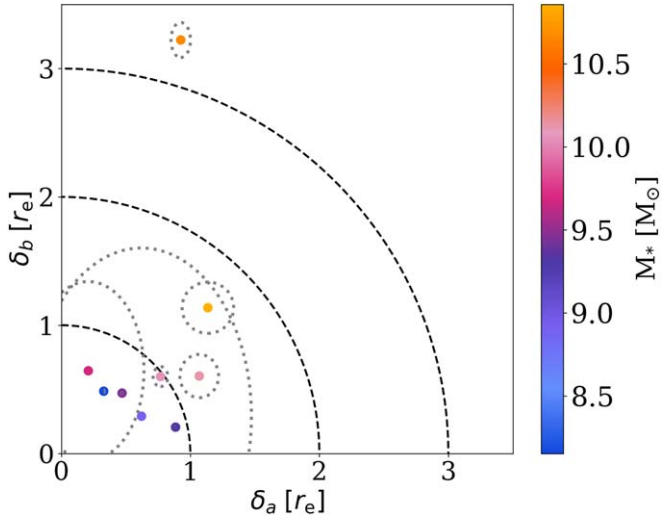

Figure 1. Locations of the FRB sample relative to their host-galaxy centroids along the major (δ_a) and minor (δ_b) axes in units of r_e, defined by the half-light radius determined by `galfit`. The gray dotted ellipses around each of the points show the FRB localization error relative to the size of the host (several are smaller than the symbols). In the case of FRB 20190711A, the FRB localization is almost 2 times the effective radius of the host, resulting in a fairly large ellipse around the central point. FRB 20191001A is highly offset along the minor axis ($\delta b \approx 3$), but less so along the major axis ($\delta a \approx 1$); see images in Mannings et al. (2021). The points cluster at δ_a, $\delta_b < 1.5 r_e$. Therefore, the bursts are predominantly within the inner disks of the galaxies but rarely (if ever) from the nucleus itself (i.e., $<< r_e$).

Mannings et al. (2021) characterizes the FRB locations in that sample as occurring at moderate offsets on or near spiral-arm structure. Bhardwaj et al. (2021) shows that FRB 20201001E likely originated in a globular cluster in the outskirts of M81. In contrast, FRB 20121102A occurs very near a central star-forming region in its host. Therefore, as regards the ISM contribution to the RM, one expects variation as the bursts occur in relatively diverse environments, although the majority are located on or near spiral structure.

We also characterize the host galaxies in the sample according to their overall properties. In Figure 2, we compare the global properties of the host galaxies in the sample against measurements of field galaxies at similar redshift. In the bottom panel, we show a color–magnitude diagram where hosts in the "Blue" region are early-type galaxies with young stellar populations and active star formation, while those in the "Red" region are late-type hosts with very low star formation and older stellar populations. The majority of these FRB hosts are star-forming and lie either in the so-called blue cloud of galaxies or the green valley, as supported by what is shown in the upper panel (the star formation rate versus stellar mass diagram), where most of the hosts reside in the "star-forming" region of the plot. The two notable exceptions are FRB 20200120E and FRB 20180916B, which have hosts with nonzero SFR but lie below the SFR main sequence. The figure indicates that the galaxies studied here have properties typical of a $z \sim 0.2$ population with a preference for star-forming and more luminous/massive galaxies. For the full parent population of FRB host galaxies, however, Safarzadeh et al. (2020) demonstrated that the hosts are less massive (and have lower SFR) than a sample weighted by SFR. The points are colored by the extragalactic RM (RM$_{\rm EG}$; see Equation (5)), but there is no apparent correlation between the host properties and RM$_{\rm EG}$.

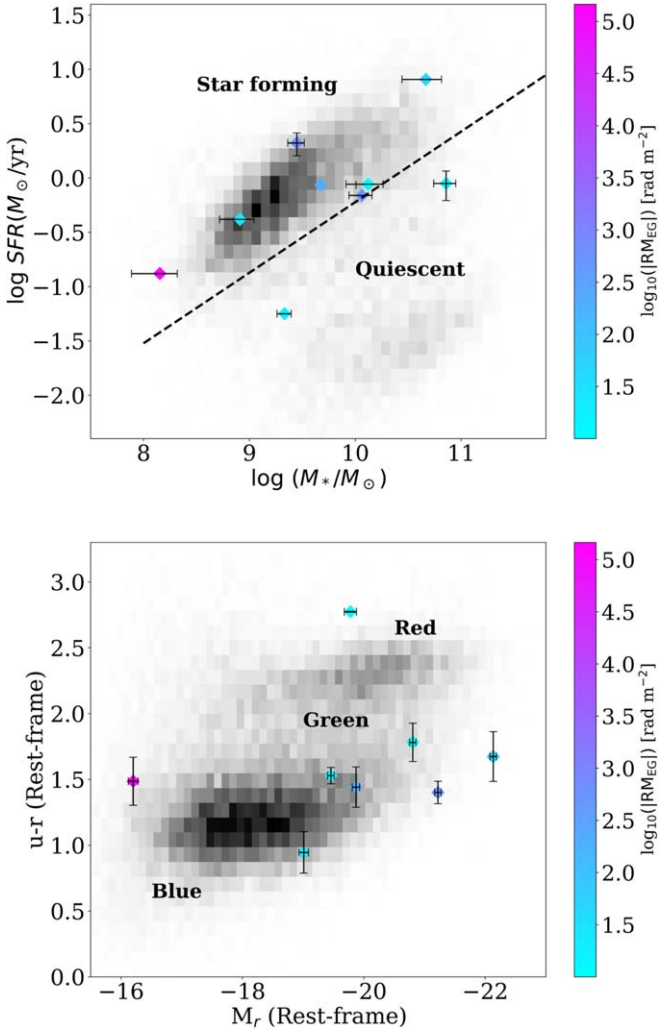

Figure 2. Top: diamond points (colored by $\log_{10}|{\rm RM_{EG}}|$; the RM component excluding Milky Way contribution; see Section 3.1.1) present the global measures of stellar mass (M_*) and star formation rate (SFR) for the host galaxies of our RM sample. The dashed line divides quiescent and star-forming hosts, and the 2D histogram describes the distribution for field galaxies from the PRIMUS survey (Moustakas et al. 2013). The majority of hosts lie in the star-forming region of the diagram, with two in the quiescent region. Bottom: color–magnitude diagram with points and histogram as above. The labels "Blue," "Green," and "Red" specify, in turn, blue galaxies thought to be currently star-forming with younger stellar populations, green hosts transitioning out of star formation, and "red and dead" galaxies where star formation has ceased and older stellar populations dominate the host. The majority of our sample populate the blue cloud or green valley, indicative of moderate star formation.

3. Observational Analysis and Results

In this section, we analyze the RM measurements to search for correlations with the host-galaxy properties and to estimate the underlying magnetic fields within the hosts. We begin by introducing approaches to isolate the RM and DM contributions from the host.

The host and burst characteristics for FRB 20121102A are anomalous in comparison to the rest of the sample, as the host is a star-forming dwarf with a persistent radio source, and the burst's RM$_{\rm FRB}$ is orders of magnitude higher than other bursts in this sample. Much attention has been given to FRB 20121102A with respect to its high RM$_{\rm FRB}$, in an attempt to determine what connection this value has to possible progenitor channels and local magnetic field properties.

It should be noted that the RM_{FRB} of 20121102A is not completely unique, with the detection of FRB 20190520B (Zhao & Wang 2021; Niu et al. 2022), whose DM_{FRB} and RM_{FRB} are both much higher than what has been observed with other bursts. The RM_{FRB} varies substantially, but reaches a maximum $>1.3 \times 10^4$ rad m^{-2} (Anna-Thomas et al. 2023), and the progenitor argued to be embedded in a combined magnetar wind nebula and supernova remnant (Zhao & Wang 2021). We include FRB 20121102A in our analysis despite its extreme RM, but, where relevant, we comment on results without its inclusion.

3.1. Constraining the Contribution to RM_{FRB} from the Intergalactic Medium

In this subsection, we search for any trend of RM_{EG} with redshift akin to the Macquart relation for the DM.

In this case, we do not expect a trend with redshift since there is no expected preferred direction of magnetic fields on cosmic scales. The random orientation of these intergalactic fields, and probable dominance of the turbulent field components, lead to field reversals along what can be considered to be a random walk, where the mean field is $\langle B \rangle \sim 0$, while $\sigma_B^2 \ggg 0$. Therefore, integrated along the line of sight, $B_\parallel$ approaches zero on average (Section 1.1). We first, however, describe our approach to removing an estimated contribution to RM_{FRB} from our Galaxy.

3.1.1. Milky Way Rotation Measure (RM_{MW})

Each of the RM_{FRB} measurements include a contribution from the path through our Galaxy. This includes both the interstellar medium (ISM) and any halo component.

The Faraday map presented in Oppermann et al. (2012) uses surveys of polarized extragalactic radio sources to determine RMs within and outside of the Galactic plane.

This model's methodology and theoretical framework are used as a basis for the production and improvement of the HE20 model (Hutschenreuter & Enßlin 2020; Hutschenreuter et al. 2022), a Faraday sky model that uses the correlation between Galactic Faraday rotation and Galactic free–free emission to increase the accuracy of previously developed maps (Hutschenreuter & Enßlin 2020). They also incorporate a new all-sky data set, which has a higher density of sources near the Galactic plane and other underresolved areas of the sky (such as the southern sky). These improvements increase the resolution of the resulting maps by a factor of 2 over previous studies (Hutschenreuter et al. 2022).

Therefore, we use the HE20 model of RM_{MW} to account for the Milky Way's contribution to RM_{FRB} to thereby isolate the extragalactic RM contribution:

$$RM_{EG} = RM_{FRB} - RM_{MW}. \quad (5)$$

Last, we note that maps such as these are limited in their spatial resolution in regards to particular lines of sight through the Milky Way. However, the HE20 model uses a total of 55,190 sources (primarily from the LOFAR Two-meter Sky Survey and NRAO VLA Sky Survey RM catalogs), resulting in improvements in resolution and uncertainties. The uncertainties mostly range from 80 rad m^{-2} in the plane of the Galaxy to ~ 0 rad m^{-2} as we move to lines of sight further from the disk. There are few regions in the Galactic plane (specifically toward Galactic center) where the uncertainties reach $\simeq 300$ rad m^{-2} (Hutschenreuter et al. 2022), but none of our FRBs have lines of sight near $|l| \sim 0°$.

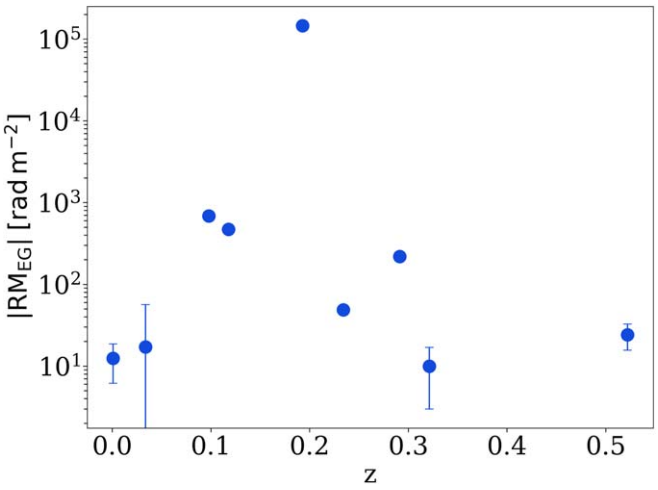

Figure 3. Amplitude of the extragalactic rotation measure ($|RM_{EG}|$) as a function of redshift (z) for the full set of FRBs in this sample. Error bars are shown, where some errors are smaller than the points. There is no significant correlation between the two, in sharp contrast to the burst DM, which shows a clear dependence on redshift (evidenced in the Macquart relation; Macquart et al. 2020; James et al. 2022). This indicates no strong influence from intergalactic magnetic fields and that the local environment (host and immediate burst environment) dominates $|RM_{EG}|$. The extremum of the $|RM_{EG}|$ distribution is FRB 20121102A, which is expected to reflect a highly magnetized environment in which the burst resides.

3.1.2. Correlating RM_{EG} with z

Figure 3 plots the absolute value of the extragalactic RM_{EG} for each sight line against the FRB redshift. There is no discernible trend between these two quantities. Both parametric (slope of the best-fit line) and nonparametric (Spearman) tests reveal no significant correlation. This stands in stark contrast to the strong correlation observed between DM and redshift (the Macquart relation), which arises from the highly ionized cosmic web (Macquart et al. 2020). The absence of any apparent correlation in Figure 3 implies the IGM makes little contribution to the overall RM, primarily due to reversals in the magnetic field over cosmic scales. This is consistent with upper limits for the contribution of intervening galaxy halos (Lan & Prochaska 2020).

For the remainder of the paper, we assert that the cosmic contribution to RM_{FRB} (RM_{cosmic}) is negligible. Therefore RM_{FRB} is dominated by only two components along the sight line, our Galaxy and the FRB host. In turn, this implies RM_{EG} is dominated by the host contribution and, given Equation (5), we have

$$RM_{host} \approx (RM_{FRB} - RM_{MW})\,(1+z)^2, \quad (6)$$

which explicitly applies a factor of $(1+z)^2$ to correct to the host rest frame. In what follows, we test Equation (6) and then derive estimates for the magnetic field strength of the FRB host galaxies based on its evaluation.

3.2. Estimating the Host Dispersion Measure (DM_{host})

In Section 3.1.2, we argued that the extragalactic RM (RM_{EG}) estimates for the FRBs arise from ionized and magnetized gas within their host galaxies. Adopting this expectation, we may leverage observations of the galaxies and

Table 3
Estimated RM, DM, and Magnetic Field of the Host Galaxies

FRB	RM_{host} (rad m^{-2})	RM_{MW} (rad m^{-2})	$DM_{host}^{H\alpha}$ (pc cm^{-3})	DM_{host}^{UV} (pc cm^{-3})	$DM_{host}^{Macquart}$ (pc cm^{-3})	$\lvert B_{\parallel}\rvert$ (μG)
20121102A†	146127 ± 137	-18 ± 37	183	3519	231 ± 99	777 ± 366
20180916B†	-17 ± 40	-99 ± 39	167		113 ± 48	0.19 ± 0.43
20180924B	10.0 ± 7.0	16.3 ± 5.0	311	<117	-3 ± 205	0.4 ± 2.8
20190102C	-219.5 ± 8.7	26.6 ± 7.7	177	<202	17 ± 163	9 ± 54
20190608B	472 ± 15	-24 ± 13	135	154	181 ± 28	3.2 ± 1.1
20190711A†	-24.2 ± 8.5	19.4 ± 6.5		<173	34 ± 333	0.9 ± 9.2
20191001A	48.8 ± 5.2	23.5 ± 4.3	512	<116	272 ± 126	0.22 ± 0.11
20200120E†	-12.4 ± 6.3	-17.4 ± 5.8			7 ± 4	0.51 ± 0.26
20201124A†	-686 ± 26	-44 ± 24	810		181 ± 2	4.7 ± 1.2

Notes. Daggers denote repeating FRBs. $DM_{host}^{Macquart}$ for FRBs 20180924B, 20190102C, and 20200120E are all below 30. For the calculation of $B_{\parallel}$, we set a minimum DM of 30 pc cm^{-3}, but report the derived values here. Those left blank do not have the necessary measurements to calculate DM_{host} using the particular method.

the local environments of the FRBs to provide further insight into the underlying magnetic field. In particular, we aim to provide an order-of-magnitude estimate for the magnetic field strength. Following standard treatment for sight lines through the Galactic ISM (e.g., Arshakian et al. 2009; Beck et al. 2019), one requires an estimate for the DM of the gas giving rise to RM_{host} to calculate $|B_{\parallel}|$. We will also use this DM estimate to guide the models of RM_{host} presented in Section 4.

We will make the further assumption that RM_{host} is dominated by gas within the host-galaxy ISM and/or the local environment of the FRB. Specifically, we ignore any RM contribution from the diffuse and ionized gas of the host halo. This is due to the lower anticipated density of halo gas, as supported by galaxy formation theory and simulations (see Section 4). Therefore, we wish to estimate the DM of the host foreground to the FRB. We define this quantity as $DM_{host,ISM}$ and assume that $DM_{host} \approx DM_{host,ISM}$.

We consider several approaches to estimate $DM_{host,ISM}$, each of which bears significant uncertainty. One approach follows Reynolds (1977; further developed in Tendulkar et al. 2017), who introduced a method to relate the emission measure (EM, $\propto n_e^2$) to the sight line DM ($\propto n_e$) allowing for a parameterization of the unknown clumping of the gas. For the EM, we consider two observed fluxes of radiation from gas toward the FRB.

The first EM is the observed surface brightness of hydrogen recombination radiation (e.g., Hα). In its favor, the majority of FRB host galaxies have one or more optical, nebular hydrogen recombination lines measured from optical spectroscopy (e.g., Bhandari et al. 2022). On the negative side, most of these were obtained from long-slit observations centered on the host galaxy and not necessarily including the FRB location. Furthermore, the typical atmospheric seeing of $\sim 1''$ and the generally small angular sizes of the galaxies (with exceptions) yield only a characteristic surface brightness from the host-galaxy ISM. Table 3 lists a set of estimates of $DM_{host}^{H\alpha}$ based on published, integrated Hα flux measurements,[10] the angular sizes of the galaxies, and corrected for dust extinction. These range from one to many hundreds of parsecs per cubic centimeter.

For the subset of FRBs with hosts observed at high spatial resolution, we may better constrain the EM at the FRB location. Six of the nine FRBs have extant HST observations at $\approx 0.1''$ FWHM resolution (Mannings et al. 2021). These are primarily broadband images at UV and near-IR wavelengths. The UV emission is dominated by radiation from massive stars, which also drive the nebular hydrogen emission; the two are strongly correlated (e.g., Calzetti 2001). For those with UV, we use the standard scaling between near-UV luminosity and Hα luminosity (Kennicutt 1998) to estimate the Hα surface brightness from the UV observations. We then calculate the EM and relate this to a DM estimate. Table 3 lists the DM_{host}^{UV} estimates for these six galaxies.

Last, we consider a complementary approach to estimating $DM_{host,ISM}$ using the Macquart relation, which relates the cosmic dispersion measure, DM_{cosmic}, with redshift (Macquart et al. 2020). We refer to this estimation as $DM_{host}^{Macquart}$. The method is to subtract from the observed total dispersion measure, DM_{FRB}, estimates for the Galactic ISM and halo (DM_{ISM}, DM_{halo}) and the cosmic web (DM_{cosmic}):

$$DM_{host}^{Macquart} = DM_{FRB} - DM_{ISM} - DM_{halo} - DM_{cosmic}. \quad (7)$$

We use the NE2001 model (Cordes & Lazio 2003) of the Galactic ISM to evaluate DM_{ISM} for each FRB sight line and assume the Milky Way halo contributes $DM_{halo} = 40$ pc cm^{-3} (e.g., Prochaska & Zheng 2019). From the host-galaxy redshift, we calculate the average $\langle DM_{cosmic} \rangle$ (Macquart et al. 2020). This yields the $DM_{host}^{Macquart}$ values listed in Table 3, which have also been corrected to the rest frame of the host (i.e., we applied a factor of $1 + z$). Formally, these include gas from both the ISM and halo of the host galaxy; and current work suggests the host halo term may contribute several tens of parsecs per cubic centimeter (Prochaska & Zheng 2019). We also note that structure in the cosmic web lends to an asymmetric scatter about $\langle DM_{cosmic} \rangle$, and the median DM_{cosmic} value is predicted to be several tens of parsecs per cubic centimeter lower than the mean. These two corrections offset against one another, and we therefore proceed with Equation (7) for our $DM_{host}^{Macquart}$ estimates acknowledging that these bear ~ 30 pc cm^{-3} uncertainty.

Inspecting the values of $DM_{host,ISM}$ listed in Table 3, one notes each approach exhibits a distinct distribution. The $DM_{host}^{H\alpha}$ estimations span the largest range and exhibit the largest values. Indeed, many exceed $DM_{host}^{Macquart}$ and even the total DM_{FRB} of the sight line. The dust-corrected DM_{host}^{UV} distribution are primarily upper limits of 100 to a few hundreds of parsecs per cubic centimeter and are generally consistent with $DM_{host}^{Macquart}$. We proceed with analysis that adopts $DM_{host}^{Macquart}$

[10] Or Hβ converted to Hα using standard nebular flux ratios.

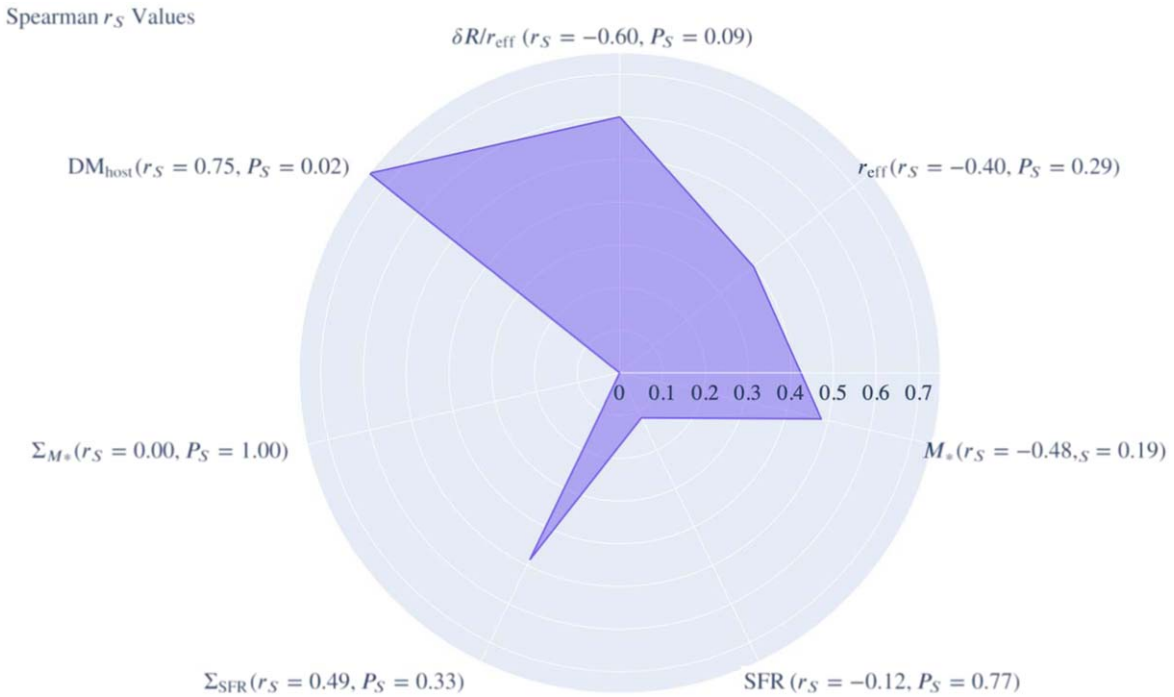

Figure 4. A radar plot showing Spearman r_S values as tests for the correlation between absolute rotation measure (|RM|) and a range of galaxy-scale and local-environment-related measures. The radial values represent the absolute value of the stated r_S values, and the associated significance measures are shown as well. A negative r_S represents anticorrelation. The only correlation meeting our significance criterion ($P_S < 0.05$) is that with DM$_{\rm host}$. This positive correlation can naturally arise from the fact that both quantities are sensitive to the electron density in the host ISM.

for the host DM; however, two of the values calculated for $\mathrm{DM}_{\rm host}^{\rm Macquart}$ are $\sim$1 or negative. Therefore, we impose a minimum value of 30 pc cm^{-3} based on the minimum value of our own Galactic ISM (NE2001), noting that all of the galaxies exhibit signatures of star formation and must harbor a nonnegligible ISM. This minimum value also accounts for uncertainty in the methodology. For completeness, the values presented in Table 3 show the calculated values for $\mathrm{DM}_{\rm host}^{\rm Macquart}$ including those which are below this minimum. However, the minimum threshold is implemented in all subsequent analyses.

3.3. Correlating Host Characteristics with Rotation Measure

We now test for correlations between global and local characteristics of the host galaxies and RM isolated to the host galaxy (i.e., with the Galactic component subtracted using Equation (6); RM$_{\rm host}$). To the extent that RM$_{\rm host}$ traces gas beyond the local environment, we may identify correlations with the host-galaxy properties. For example, one may expect FRBs found in regions of elevated star formation to exhibit a higher RM. Magnetic fields get wrapped up into forming stars, but the fields can also be amplified by ionizing radiation and turbulence from violent star formation, cloud collapse, and massive star death.

Specifically, we consider global measures of the star formation rate (SFR), stellar mass (M_*), and galactocentric offset (relative to the galaxy effective radius, $\delta R/r_e$). We also consider local measures of the SFR and M_* surface densities ($\Sigma_{\rm SFR}$, Σ_{M*}; Table 1) and our estimate of DM$_{\rm host}$, which would include both local and ISM contributions.

We perform Spearman tests, computing Spearman correlation coefficients r_S, with the null hypothesis that there is no correlation between RM and a given measurement. We select the Spearman test because there is no assumption of Gaussian distributions for the variables. We perform the analysis in log–log space (as opposed to linear space) as the power-law relationships appear linear, and many of these values span several orders of magnitude. Last, we set a threshold of the Spearman probability for a significant correlation at $P_S < 0.05$ (i.e., requiring 95% significance).

The absolute values of the resultant r_S values are shown in Figure 4. Although there are a number of parameters for which $|r_s| > 0.5$, the condition for significance is only satisfied for one quantity: DM$_{\rm host}$. A positive correlation between DM$_{\rm host}$ and RM$_{\rm host}$ is in line with expectation because both quantities depend on the electron density of the host ISM. The correlation also lends further support to the assertion that RM$_{\rm EG}$ is dominated by RM$_{\rm host}$.

The next strongest correlation is an anticorrelation between RM$_{\rm host}$ and $\delta R/r_e$, although with $P_S > 0.05$. This trend follows observed and simulated inverse relationships between $|B_{\parallel}|$ and radius (e.g., Wielebinski & Beck 2005; Pakmor et al. 2017). We await future observations to confirm (or refute) such a trend in FRB observations.

As our sample is limited a sample size of nine FRBs, such tests should be repeated with greater confidence with a larger sample size. One also notes that the significance of these analyses is reduced by a trials-factor penalty incurred when testing for multiple correlations.

3.4. B-field Estimation

As stated in Arshakian et al. (2009), the RMs of polarized background sources can be used to reconstruct a host or intervening galaxy's magnetic field topology. FRB signals have since been shown to be one such source. FRBs and their RMs can reveal the orientation and magnitude of ordered magnetic fields, making them a powerful tool. Here, we look at the

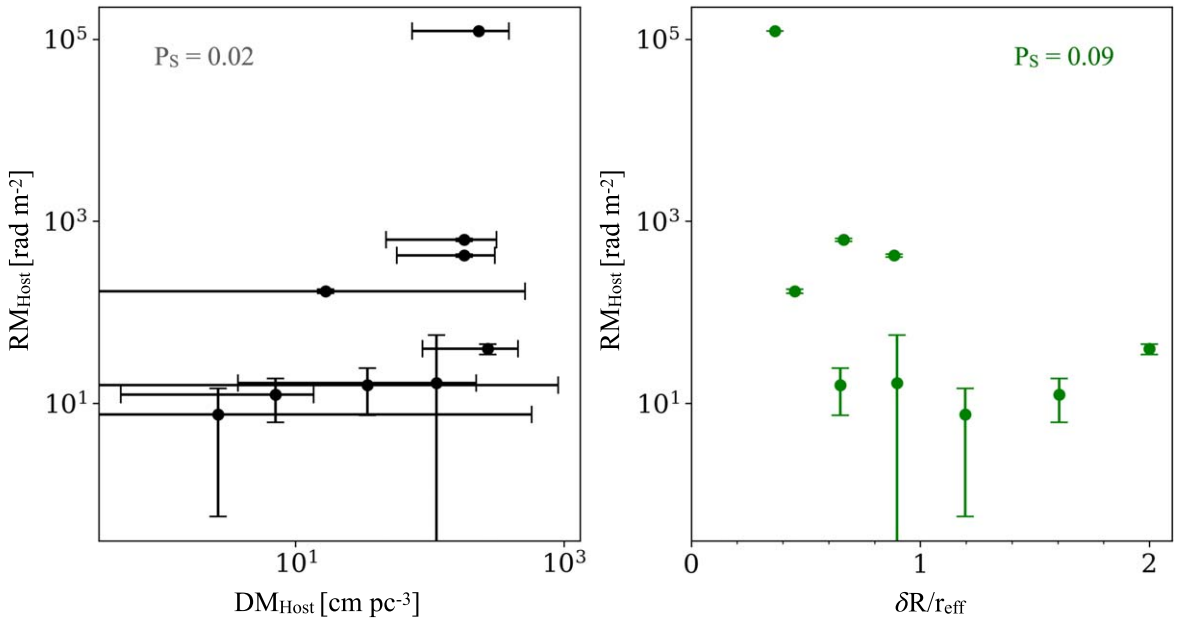

Figure 5. RM_{host} as functions of DM_{host} (left, black) and $\delta R/r_e$ (right, green), with associated P_S values. We can see a positive correlation by eye between RM_{host} and DM_{host}; however, a correlation between RM_{host} and $\delta R/r_e$ is not as apparent.

power of FRB sight lines to provide insight on the fields of the galaxies that host well-localized bursts.

As defined, RM is the sight-line integral of the parallel component of the magnetic field weighted by the electron density. Therefore, the ratio of RM-to-DM (the unweighted n_e integral) yields an estimate of the magnetic field, after accounting for differences in the prefactors (e.g., Akahori et al. 2016; Pandhi et al. 2022):

$$\langle B_{\parallel} \rangle \approx \frac{C_D \mathrm{RM}}{C_R \mathrm{DM}} = 12.3 \left(\frac{\mathrm{RM}}{10 \text{ rad m}^{-2}} \right) \left(\frac{\mathrm{DM}}{10^3 \text{ pc cm}^{-3}} \right)^{-1} \mathrm{nG}, \quad (8)$$

with C_D and C_R constants equal to 1000 and 811.9, respectively. In Akahori et al. (2016) they propose (with some improvements to Equation (8)) that many measurements of RM_{FRB} and DM_{FRB} can provide the data necessary to probe intergalactic magnetic fields (IGMFs). This estimation also assumes a constant magnetic field and that there is no correlation between n_e and $B_{\parallel}$, whereas it is possible the magnetic field strength will likely decrease exponentially with radius and height in the disk (similar to n_e). These effects should be less than an order of magnitude, making the given ratio sufficient for estimating the magnitude of the magnetic fields in our sample's host galaxies. Furthermore, we adopt values of RM_{host} and DM_{host} to isolate the magnetic field estimation to within the host galaxy.

Considering the turbulence and ionization due to active star formation and the deaths of massive stars, one may suspect a relationship between star formation rate and the magnitude of magnetic fields in the host. We also investigate the relationship between stellar mass and magnetic field strength. In Rodrigues et al. (2018), for galaxies at $z = 0$, they find a slight positive correlation between galaxy mass and magnetic field, but note that this correlation is broken by a number of lower-mass hosts with much higher magnetic field strengths. In Figure 6, we do not see a clear trend with strength $|B_{\parallel}|$ as a function of mass nor star formation rate, in contrast to the predictions of Rodrigues et al. (2018). FRB 20121102A exhibits the highest RM of all the bursts, but resides in the lowest-mass host. This is indicative of the highly magnetized environment that the burst progenitor lives within (Michilli et al. 2018).

In most cases, the magnetic field strengths estimated are lower than values quoted for the Milky Way ($\approx 6\,\mu$G in the outer reaches of the Galaxy and $30\,\mu$G in the inner region toward the bulge). These Galactic values are dominated by the small-scale random fields, which contrasts the regular fields along the line of sight that dominates RM. Comparing these two sets of measurements allows us to make distinctions between the strengths of various field components. We note that the values we have determined are largely consistent with $\simeq$microgauss field magnitudes, which is broadly accepted as the general magnitude of large-scale regular fields measured in galactic disks (Beck et al. 2019).

4. Modeling Galactic Magnetic Fields

4.1. Auriga Model

To gain a better understanding of the physical mechanisms that can influence the magnetic fields in the host galaxies of our observed FRBs, we compare them to similar galaxies in the Auriga simulations.

The Auriga simulations are a set of cosmological magneto-hydrodynamical zoom-in simulations of Milky Way–like galaxies (Grand et al. 2017). They model magnetic fields in the approximation of ideal magnetohydrodynamics (MHD) using a second-order finite-volume scheme (Pakmor et al. 2011; Pakmor & Springel 2013) in the AREPO code (Springel 2010; Pakmor et al. 2016; Weinberger et al. 2020). The magnetic field is initialized at $z = 127$ as a uniform magnetic seed field with a strength of 1.6×10^{-10} physical G. The simulation then evolves the magnetic field self-consistently until $z = 0$.

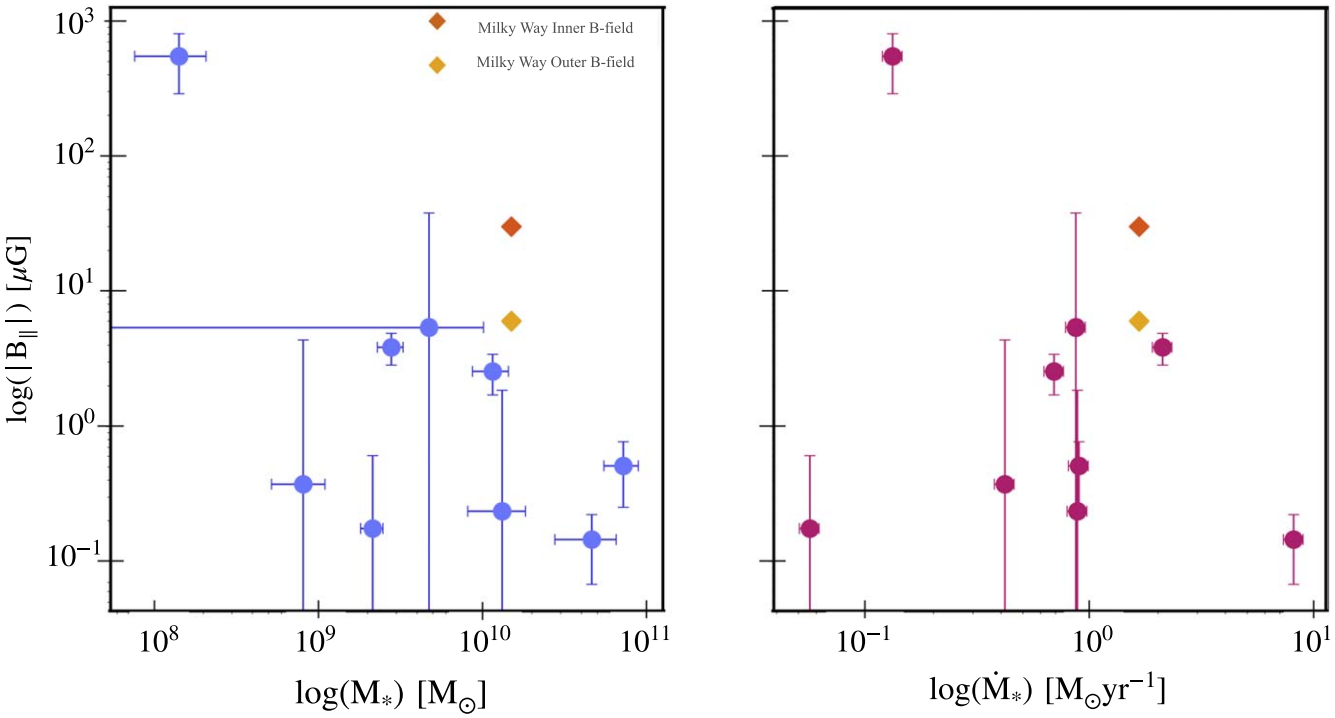

Figure 6. Comparison of the magnitude of the $B_{\parallel}$ component of the magnetic field to stellar mass (right panel) and star formation rates (left panel). We also show values determined for the Milky Way (Wielebinski & Beck 2005), for the bulge/inner field in *yellow* and the disk/outer field in *orange*, using values for mass and star formation rate found in Fragione & Loeb (2017) and Licquia & Newman (2015), respectively. We find no apparent correlations between these global galactic characteristics and magnetic field measurements in this sample of FRB hosts.

When the galaxies first form, the magnetic field is quickly amplified via a turbulent small-scale dynamo and saturates before $z = 4$ with a magnetic energy density that reaches ∼10% of the turbulent energy density and erases any information about the seed field in the galaxy (Pakmor et al. 2014). After the galaxies form a disk at $z < 2$, the differential rotation in the disk leads to a second phase of magnetic field amplification that ends when the magnetic energy density reaches equipartition with the turbulent energy density (Pakmor et al. 2017). The magnetic field properties, synthetic Faraday rotation maps, and the magnetic field in the CGM of the Auriga galaxies have been shown to be consistent with observations (Pakmor et al. 2016, 2018, 2020).

The Auriga simulations focus on a Lagrangian high-resolution region with a typical radius of 1 Mpc/h around the central Milky Way–mass galaxies. This high-resolution region contains a large number of smaller galaxies without contamination from low-resolution dark matter particles that we also include in our sample here. We focus our analysis on the six high-resolution simulations of the Auriga project with a baryonic mass resolution of ≈ 7–$8 \times 10^3\, M_{\odot}$. These are supplemented by yet-unpublished simulations with the same mass resolution, centered on lower-mass galaxies ($M_{\rm halo} = 10^{10}$–$10^{11.5}\, M_{\odot}$) for which the high-resolution regions also extend to about 5 times the virial radius around each central galaxy.

4.2. Host and Sight-line Selection

We first find galaxies in our simulation suite with stellar mass, star formation rate, and effective radius consistent with the host galaxies of our FRB sample. We calculate the stellar mass of a simulated galaxy by including all stars within 3 times its stellar half mass–radius. Its star formation rate is averaged over the last 100 Myr using newly formed stars within the same radius. We use the stellar half mass–radius as a proxy for the effective radius. We include all galaxies (both central and satellite galaxies) that match the FRB sample to within twice the observational error. For the effective radius, however, we add a 10% error in quadrature to the observational error, because in some cases the derived errors were so small that no match could be found. With this selection procedure, we found one or more matching galaxies for seven out of the nine observed host galaxies.

We tilt each of the galaxies into the observed inclination and then integrate the RM and DM values for 256 different lines of sight. The starting point of each line of sight is the position of a random star particle with an age younger than 200 Myr. The frequent incidence of FRBs on or near spiral arms could indicate the association of FRBs with relatively young stellar populations. From the starting point, we integrate each line of sight until it reaches an observer at a distance of 100 kpc. We checked that increasing the integration distance does not change our results.

The local electron density for the integration along the line of sight is computed exactly as described in Pakmor et al. (2018), in particular assuming that only the volume-filling warm phase of the ISM contributes and that this phase is fully ionized. The magnetic field is taken directly from the simulation.

4.3. Correlation between Dispersion Measure and Rotation Measure

We show the correlation between RM and DM for all sight lines we computed from the Auriga galaxies in Figure 7. RM and DM are clearly strongly correlated, as expected. However, there is significant scatter, i.e., for a fixed DM value the RM value can vary by 2 orders of magnitude. Nevertheless, the

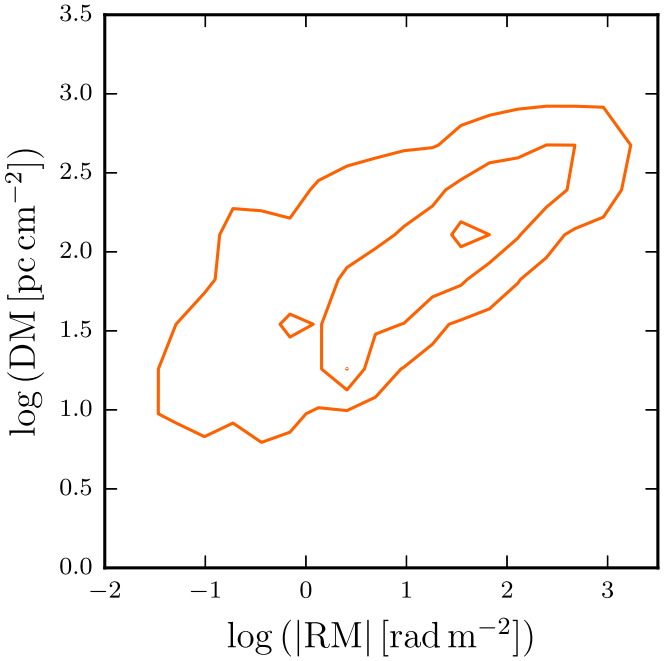

Figure 7. Correlation between RM and DM values for lines of sight from matched host galaxies in Auriga. We show 10%, 50%, and 90% contours of the distribution. Although there is nonnegligible scatter, the RM and DM are strongly correlated in the simulations.

scatter is small on the scale of the overall variation of 5 orders of magnitude in DM and 8 orders of magnitude in RM.

Motivated by the strong correlation between DM and RM, we not only compare the RM distributions of all lines of sight of matched FRB host galaxies, but also compare to a subsample of lines of sight that show consistent DM values.

4.4. Dispersion Measure and Rotation Measure of Matched Auriga Galaxies

We show the distribution of RM (purple lines) and DM (red lines) values for 256 lines of sight each of all galaxies in our sample consistent with the properties of the FRB host galaxies in Figure 8. We also show the measured values as vertical lines of the same color.

Strikingly, the shape of the distributions of synthetic DM and RM values match for most FRBs. The RM and DM distributions overlap with the values inferred for the FRB host galaxies from our observations, with the exception of FRB20201124A. Median values and 95% confidence intervals are shown in Table 4.

We also show the RM distributions restricted to lines of sight that have a DM value consistent with the observed host-galaxy DM ($\mathrm{DM_{sim}} < \max(100\ \mathrm{pc\ cm^{-3}}, 2 \times \mathrm{DM_{host}^{Macquart}})$, shown by the dashed, yellow curves). For most FRBs, this restricted RM distribution is essentially the same as the full RM distribution. For FRB20190102C, FRB20201124A, and FRB20190711A this restriction reduces the high RM tail of the distribution. Interestingly, in all three cases the host RM estimated from observations lies on this tail that is reduced significantly by the restriction on DM. We also note (as seen in Figure 8) the noticeable difference between the modeled probability density function (pdf) and observed $\mathrm{RM_{host}}$ for FRB20190608B, though, again, the value lands on the tail of the distribution. This could point to an nonnegligible contribution of the local environment to the observed RM, as was discussed in Chittidi et al. (2020). The authors point out the high RM in comparison to other bursts such as FRB 20180916, implying a magnetized local environment.

A larger sample is necessary to determine whether or not these variations are truly due to local effects.

An extreme exception is FRB20121102A. We do not find any lines of sight that have an RM value even remotely comparable to the large observed value. In contrast, the DM value is barely consistent with our synthetic lines of sight. This indicates that the magnetic field dominating the RM of FRB20121102A is part of its local stellar environment that is not included in our simulations. Michilli et al. (2018) discusses this highly magnetized local environment.

Note, also, it is likely that increased scatter broadening of the FRB signal would bias against FRBs being detected with high host DM contribution.

5. Discussion

This sample represents the largest collection of FRB RMs presented with accompanying high-precision localizations and follow-up imaging of the associated hosts. A majority of the hosts in this sample are massive, star-forming galaxies at $z < 0.5$, with a few exceptions at lower mass or SFR.

To explore the relationships between FRB RMs and host characteristics, we first isolated the extragalactic contribution to the RM ($\mathrm{RM_{EG}}$). We used the Galactic Faraday rotation map developed in Hutschenreuter et al. (2022) and found no correlation between $\mathrm{RM_{EG}}$ and z. This is consistent with measurements of the IGMF found in Carretti et al. (2022), which follows from an expected random nature and much lower strength of the fields in the IGM.

We therefore disregarded IGMF contributions and assert that $\mathrm{DM_{EG}}$ is dominated by the RM of the host-galaxy $\mathrm{DM_{host}}$. We find a strong correlation between $\mathrm{RM_{host}}$ and $\mathrm{DM_{host}}$, which supports this assertion and provides encouraging confidence that FRBs probe the magnetic fields of their host galaxies. This correlation is expected if the magnetic field has a significant ordered component that only varies weakly along the line of sight. Then both quantities depend similarly on the integrated density of the ionized medium along the line of sight through the host galaxy. This is consistent with our observational and theoretical picture of magnetic fields in massive disk galaxies (Beck 2015; Pakmor et al. 2017).

There is evidence for an anticorrelation between host-normalized galactocentric offset and $\mathrm{RM_{host}}$ but at less than 95% confidence. A larger data set is required to test whether FRBs reveal this relationship, though observed and modeled field strengths have been seen to show some radial dependence.

We considered several methods to isolate the host contribution to the dispersion measure, $\mathrm{DM_{host}}$, relating the emission measure to DM (Reynolds 1977) and applying the Macquart relation (Macquart et al. 2020) to estimate $\mathrm{DM_{host}}$. We then use the relation between DMs and RMs described in papers such as Akahori et al. (2016) and Pandhi et al. (2022) to make an estimate of $B_{\parallel}$ for each of our host galaxies.

With this method, we find magnetic field strength estimates for our sample of the order of $\sim 1\ \mu$G. The estimate, however, disregards field reversals of the magnetic field along the line of sight as well as differences in the exponential scaling of the magnetic field strength and electron densities with radius and height in the disk. Therefore, although the values are lower than values quoted for the Milky Way (see Figure 6), they are

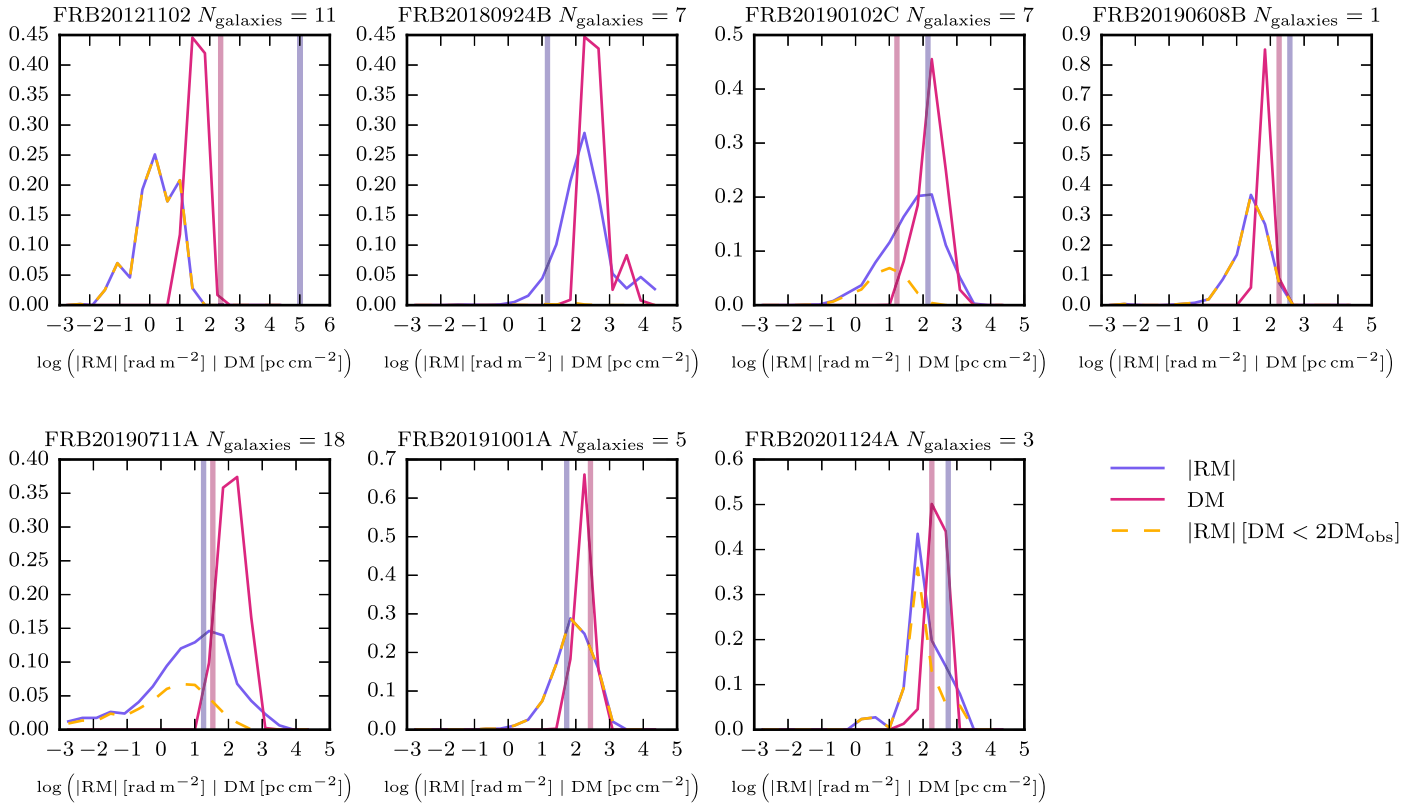

Figure 8. RM and DM distributions for lines of sight from matched host galaxies in Auriga. The name of the matched FRB host and the number of matching Auriga galaxies found are listed above each panel. Shown are histograms of the DM values (solid red lines) and absolute RM values (solid purple lines) along each line of sight. The vertical red and purple lines indicate the observed or derived $\mathrm{RM_{host}}$ and $\mathrm{DM_{host}^{Macquart}}$ values. We also show histograms of absolute RM values that include only lines of sight with a consistent DM value (dashed yellow lines; absent in panels where no consistent DM was found). The RM distributions predicted from the Auriga galaxies are generally in good agreement with the observed values, with the glaring exception of FRB20121102A whose RM value is far away from any lines of sight we find in Auriga. The modeled RM pdf for FRB20190608B is also noticeably lower than the observed value. The derived $\mathrm{DM_{host}^{Macquart}}$ value for FRB20180924B is negative; therefore, there is no vertical line shown here.

Table 4
Estimated RM, DM, and Magnetic Field of the Host Galaxies

FRB	RM Median (rad m^{-2})	DM Median (pc cm^{-3})	RM95%Interval (rad m^{-2})	DM95%Interval (pc cm^{-3})
20121102A†	2.02	2.02	[0.04, 18.56]	[0.04, 18.56]
20180916B†				
20180924B	146.22	57.31	[6.01, 12598.00]	[4.20, 117.59]
20190102C	53.55	7.24	[0.63, 1055.81]	[0.28, 69.17]
20190608B	25.84	25.84	[1.80, 120.41]	[1.80, 120.41]
20190711A†	8.58	1.66	[0.00, 745.50]	[0.00, 97.79]
20191001A	77.71	77.71	[3.40, 635.87]	[3.40 ,635.87]
20200120E†				
20201124A†	86.13	67.51	[2.83, 837.41]	[2.04, 789.91]

Notes. Daggers denote repeating FRBs. The data included here are taken from the Auriga simulations. No matches were found for FRBs 20180916B and 20200120E; thus, they have been left blank.

better seen as lower limits and are fully consistent with general expectations for galactic magnetic field strengths (Beck 2015). The uncertainty in our determinations of $\mathrm{DM_{host}^{Macquart}}$ could have some effect on the derived $B_{\parallel}$, but would not cause a notable increase.

Four (possibly five) of the hosts in this sample exhibit spiral structure, and the bursts originate on or near the spiral arms. According to Beck (2015), the strongest ordered fields are found in inter-arm regions due to shear caused by differential rotation and a large-scale dynamo that operates preferentially in the inter-arm regions. Because of the preferred location of FRBs on/near spiral arms, it is possible that our field strengths are referring to medium-scale (∼1 kpc) regular fields that are affected by turbulence in the spiral arms. Figure 9 shows where our measurements lie with respect to lines of constant $B_{\parallel}$ of varying magnitudes (with the values we derived shown in Table 3). These values align well with the average strengths of large-scale regular fields (on scales of 5–10 kpc; Beck et al. 2019), where the large-scale rotation sets the strength and structure of the magnetic field.

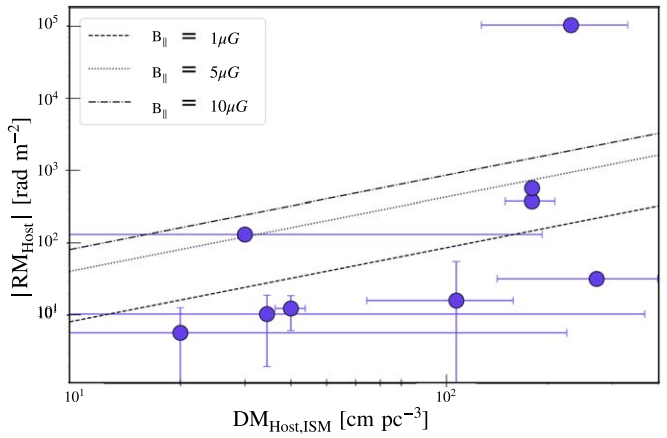

Figure 9. RM_{host} and $DM_{host,ISM}$ with lines of constant magnetic field strength (1 μG, dashed; 5 μG, dotted; 10 μG, dashed–dotted). We calculate the value of $B_{\parallel}$ for each of the FRBs using Equation (8). The majority of the values are less than 5 μG, with many even falling below 1 μG. There is one outlier, with a field magnitude far exceeding 10 μG. These values are relatively consistent with microgauss fields, but are at the lower end of the range of 1–15 μG.

Using forward modeling of cosmological simulations instead, we also find that observed RM_{host}, and therefore $B_{\parallel}$, are consistent with the Auriga simulations (see Figure 8). There is the notable exception of FRB 20121102A, which we know is embedded in a highly magnetized environment. The predicted RMs for this FRB were not able to approach the observed value, as any contribution from local environments was not included. This provides some hope that, with a sufficient number of FRBs with polarization data and ∼milliarcsecond localizations, we will be able to disentangle the ISM and local-environment contributions to the RM, and provide constraints on each.

Limiting the simulated sight-line selection to those more consistent with the observed DM for each burst reduces the tail toward high RM values of the predicted RM distribution for three of the galaxies. Although the distribution is still consistent with the observed values, the majority of predicted RM values fall below the observed ones. This could imply a nonnegligible contribution from the local stellar environment of the FRB.

Combining FRB RM signals with measures of synchrotron polarization and estimates using galactic Zeeman effect measurements, which characterize the ISM magnetic field, may also help to disentangle the magnetic field contributions within the host galaxy.

Finally, we find insignificant correlations with extant properties such as r_e, SFR, Σ_{M*}, and M_*, shown in Figure 4. With larger, upcoming surveys, these relationships can be explored in more detail with higher statistical power. There is also no apparent relationship between FRB repetition and the host and environmental characteristics we have explored in this paper. There also seems to be little differentiation in the sample presented in Gordon et al. (2023), where they explore the overall characteristics and star formation histories of FRB hosts. This is in contrast to papers such as Pleunis et al. (2021), which point out that there are some marked differences in burst characteristics (such as bandwidth and duration) of repeating and non-repeating FRBs.

We plan to repeat and expand this study with a larger sample of more precisely localized bursts with accompanying high-resolution imaging and spectroscopy. More data would not only aid in the narrowing of possible progenitors: we can also learn about galactic magnetism and its effects on galaxy formation and evolution. With the onset of large-scale surveys such as CRAFT with the upcoming CRACO upgrade, the number of FRBs that meet these criteria will vastly increase (∼three FRBs per day!), and help to determine what, on average, the local environments of FRBs look like in terms of stellar populations, magnetism and more, and investigate (inter)galactic magnetism over cosmological time.

Acknowledgments

The authors would like to thank the referee and Rainier Beck for their helpful comments on this work. A.G.M. acknowledges support by the National Science Foundation Graduate Research Fellowship under grant No. 1842400. Authors A.G.M., J.X.P., S.S, M.R., and N.T., as members of the Fast and Fortunate for FRB Follow-up team, acknowledge support from NSF grant Nos. AST-1911140, AST-1910471, and AST-2206490. This work is supported by the Nantucket Maria Mitchell Association. This research was supported in part by the National Science Foundation under grant No. NSF PHY-1748958. N.T. acknowledges support by FONDECYT grant 11191217. R.M. S. acknowledges support through Australian Research Council Future Fellowship FT190100155. F.v.d.V. is supported by a Royal Society University Research Fellowship (URF\R1\191703). This research is based on observations made with the NASA/ESA Hubble Space Telescope obtained from the Space Telescope Science Institute, which is operated by the Association of Universities for Research in Astronomy, Inc., under NASA contract NAS 5–26555. These observations are associated with programs 15878, 16080, and 14890. Support for program numbers 15878 and 16080 were provided through a grant from the STScI under NASA contract NAS5-26555.

ORCID iDs

Rüdiger Pakmor https://orcid.org/0000-0003-3308-2420
J. Xavier Prochaska https://orcid.org/0000-0002-7738-6875
Freeke van de Voort https://orcid.org/0000-0002-6301-638X
Sunil Simha https://orcid.org/0000-0003-3801-1496
R. M. Shannon https://orcid.org/0000-0002-7285-6348
Nicolas Tejos https://orcid.org/0000-0002-1883-4252
Adam Deller https://orcid.org/0000-0001-9434-3837
Marc Rafelski https://orcid.org/0000-0002-9946-4731

References

Aggarwal, K., Budavári, T., Deller, A. T., et al. 2021, ApJ, 911, 95
Akahori, T., & Ryu, D. 2011, ApJ, 738, 134
Akahori, T., Ryu, D., & Gaensler, B. M. 2016, ApJ, 824, 105
Anna-Thomas, R., Connor, L., Dai, S., et al. 2023, Sci, 380, 599
Arshakian, T., Stepanov, R., Beck, R., et al. 2009, in Wide Field Astronomy and Technology for the Square Kilometre Array, 13
Bannister, K. W., Deller, A. T., Phillips, C., et al. 2019, Sci, 365, 565
Bassa, C. G., Tendulkar, S. P., Adams, E. A. K., et al. 2017, ApJL, 843, L8
Beck, R. 2015, A&ARv, 24, 4
Beck, R., Chamandy, L., Elson, E., & Blackman, E. G. 2019, Galax, 8, 4
Bhandari, S., Bannister, K. W., Lenc, E., et al. 2020b, ApJL, 901, L20
Bhandari, S., Heintz, K. E., Aggarwal, K., et al. 2022, AJ, 163, 69
Bhandari, S., Sadler, E. M., Prochaska, J. X., et al. 2020a, ApJL, 895, L37

Bhardwaj, M., Gaensler, B. M., Kaspi, V. M., et al. 2021, ApJL, 910, L18
Calzetti, D. 2001, PASP, 113, 1449
Carretti, E., Vacca, V., O'Sullivan, S. P., et al. 2022, MNRAS, 512, 945
CHIME/FRB Collaboration, Andersen, B. C., Bandura, K., et al. 2019, ApJL, 885, L24
Chittidi, J. S., Simha, S., Mannings, A., et al. 2021, ApJ, 922, 173C
Cordes, J. M., & Chatterjee, S. 2019, ARA&A, 57, 417
Cordes, J. M., & Lazio, T. J. W. 2003, arXiv, arXiv:astro-ph:0301598
Day, C. K., Deller, A. T., Shannon, R. M., et al. 2020, MNRAS, 497, 3335
Eftekhari, T., Berger, E., Margalit, B., Metzger, B. D., & Williams, P. K. G. 2020, ApJ, 895, 98
Fragione, G., & Loeb, A. 2017, NewA, 55, 32
Gaensler, B. M. 2009, in IAU Symp. 259, Cosmic Magnetic Fields: From Planets, to Stars and Galaxies, ed. K. G. Strassmeier, A. G. Kosovichev, & J. E. Beckman (Cambridge: Cambridge Univ. Press), 645
Gordon, A. C., Fong, W.-f., Kilpatrick, C. D., et al. 2023, arXiv:2302.05465
Grand, R. J. J., Gómez, F. A., Marinacci, F., et al. 2017, MNRAS, 467, 179
Griffiths, D. J. 2013, Introduction to Electrodynamics (London: Pearson)
Hackstein, S., Brüggen, M., Vazza, F., Gaensler, B. M., & Heesen, V. 2019, MNRAS, 488, 4220
Heintz, K. E., Prochaska, J. X., Simha, S., et al. 2020, ApJ, 903, 152
Hutschenreuter, S., Anderson, C. S., Betti, S., et al. 2022, A&A, 657, A43
Hutschenreuter, S., & Enßlin, T. A. 2020, A&A, 633, A150
James, C. W., Prochaska, J. X., Macquart, J. P., et al. 2022, MNRAS, 509, 4775
Kennicutt, Robert C. J. 1998, ARA&A, 36, 189
Kumar, P., Shannon, R. M., Lower, M. E., et al. 2022, MNRAS, 512, 3400
Lan, T.-W., & Prochaska, J. X. 2020, MNRAS, 496, 3142
Licquia, T. C., & Newman, J. A. 2015, ApJ, 806, 96
Lorimer, D. R., Bailes, M., McLaughlin, M. A., Narkevic, D. J., & Crawford, F. 2007, Sci, 318, 777
Macquart, J.-P., Bailes, M., Bhat, N. D. R., et al. 2010, PASA, 27, 272
Macquart, J. P., Keane, E., Grainge, K., et al. 2015, in Proc. of Advancing Astrophysics with the Square Kilometre Array, 55
Macquart, J. P., Prochaska, J. X., McQuinn, M., et al. 2020, Natur, 581, 391
Mannings, A. G., Fong, W.-f., Simha, S., et al. 2021, ApJ, 917, 75
Mckinven, R., Michilli, D., Masui, K., et al. 2021, ApJ, 920, 138
Michilli, D., Seymour, A., Hessels, J. W. T., et al. 2018, Natur, 553, 182
Moustakas, J., Coil, A. L., Aird, J., et al. 2013, ApJ, 767, 50
Niu, C. H., Aggarwal, K., Li, D., et al. 2022, Natur, 606, 873
Oppermann, N., Junklewitz, H., Robbers, G., et al. 2012, A&A, 542, A93
O'Sullivan, S. P., Brüggen, M., Vazza, F., et al. 2020, MNRAS, 495, 2607
Pakmor, R., Bauer, A., & Springel, V. 2011, MNRAS, 418, 1392
Pakmor, R., Gómez, F. A., Grand, R. J. J., et al. 2017, MNRAS, 469, 3185
Pakmor, R., Guillet, T., Pfrommer, C., et al. 2018, MNRAS, 481, 4410
Pakmor, R., Marinacci, F., & Springel, V. 2014, ApJL, 783, L20
Pakmor, R., & Springel, V. 2013, MNRAS, 432, 176
Pakmor, R., Springel, V., Bauer, A., et al. 2016, MNRAS, 455, 1134
Pakmor, R., van de Voort, F., Bieri, R., et al. 2020, MNRAS, 498, 3125
Pandhi, A., Hutschenreuter, S., West, J. L., Gaensler, B. M., & Stock, A. 2022, MNRAS, 516, 4739
Peng, C. Y., Ho, L. C., Impey, C. D., & Rix, H.-W. 2010, AJ, 139, 2097
Piro, A. L., & Gaensler, B. M. 2018, ApJ, 861, 150
Pleunis, Z., Good, D. C., Kaspi, V. M., et al. 2021, ApJ, 923, 1
Prochaska, J. X., Macquart, J.-P., McQuinn, M., et al. 2019, Sci, 366, 231
Prochaska, J. X., Simha, S., almannin, et al. 2023, FRBs/FRB: Release to sync with Gordon et al. 2023, v2.0, Zenodo doi:10.5281/zenodo.8125230
Prochaska, J. X., & Zheng, Y. 2019, MNRAS, 485, 648
Ravi, V., Shannon, R. M., Bailes, M., et al. 2016, Sci, 354, 1249
Reynolds, R. J. 1977, ApJ, 216, 433
Rodrigues, L. F. S., Chamandy, L., Shukurov, A., Baugh, C. M., & Taylor, A. R. 2018, MNRAS, 483, 2424
Safarzadeh, M., Prochaska, J. X., & Heintz, K. E. 2020, ApJ, 905, 30
Simha, S., Burchett, J. N., Prochaska, J. X., et al. 2020, ApJ, 901, 134
Springel, V. 2010, MNRAS, 401, 791
Tendulkar, S. P., Bassa, C. G., Cordes, J. M., et al. 2017, ApJL, 834, L7
Tendulkar, S. P., Gil de Paz, A., Kirichenko, A. Y., et al. 2020, ApJ, 908, 12
Weinberger, R., Springel, V., & Pakmor, R. 2020, ApJS, 248, 32
Wielebinski, R., & Beck, R. 2005, in Cosmic Magnetic Fields, ed. R. Wielebinski & R. Beck (Heidelberg: Springer)
Zhao, Z. Y., & Wang, F. Y. 2021, ApJL, 923, L17